Electronic Supplementary Material (ESI) for CrystEngComm.
This journal is © The Royal Society of Chemistry 2020

Multifunctional Photoelectric Sensors and Catalysts for CO_2RR and Cr(VI) Solution Based on A Series of POM-based Materials

Chen Wang, Jun Ying*, Xin-Yue Zhang, Bao-Yue Zhang, Ai-Xiang Tian and Xiu-Li Wang*

Department of Chemistry, Bohai University, Jinzhou 121013, P. R. China

Materials and General Methods

The FT-IR spectra were taken on a Varian FT-IR 640 spectrometer (KBr pellets) in the range of 400-4000 cm^{-1}. The thermal gravimetric analyses (TGA) were carried out in N_2 on a Perkin-Elmer DTA 1700 differential thermal analyzer with a rate of 10.00 ^oC/min. Powder X-ray diffraction (PXRD) patterns were recorded on an Ultima IV with D/teX Ultra diffractometer at 40 kV, 40 mA with Cu Kα (λ = 1.5406 Å) radiation in the 2θ range of 5–50°. A CHI660 electrochemical workstation was used to measure electrochemical capability and collect data. The classical three-electrode system was adopted, in which the saturated calomel electrode (SCE) was used as reference electrode and the Pt wire as the counter electrode. The title compounds were prepared as working electrodes by modifying carbon paste electrodes (**n**–CPEs). Flouromax-4NIR fluorescence spectrometer was used to measure fluorescence properties. Online gas chromatography (GC, Agilent 7890B) was used to analyze the gas products for the faradaic efficiency analysis. UV-Vis absorption spectra were obtained using a UV-1801 ultra violet spectrophotometer.

Preparation of compounds 1–5

Synthesis of $[Cu^I(dm4bt)_2]_4[GeW_{12}O_{40}]$ (1)

$CuCl_2$ (0.09 g, 0.67 mmol), $K_6Na_2[GeW_{11}O_{39}]\cdot 13H_2O$ (0.08 g, 0.026 mmol) and

* Corresponding author. Tel.: +86-416-3400158

E-mail address: ying@bhu.edu.cn (J. Ying) , wangxiuli@bhu.edu.cn (X. L. Wang).

dm4bt (0.02 g, 0.1 mmol) were dissolved in 10 mL of distilled water at room temperature. The suspension was stirred for 30 min in air, and the pH of the solution was then adjusted to about 2.5 with 1.0 mol·L^{-1} HCL. The resulting suspension was sealed in a Teflon-lined autoclave (25 mL) and kept at 150 °C for 5 days. After cooling to room temperature, orange-red block crystals of **1** (0.057 g, yield 50% based on W) were obtained and the final pH is 2.1. Anal. Calcd for **1** $C_{64}H_{64}Cu_4GeN_{16}O_{40}S_{16}W_{12}$(4743) : C 16.21, H 1.36, N 4.72%. Found: C 16.19, H 1.34, N 4.69%.

Synthesis of $[Ni_4^{II}(dm4bt)_8(GeW_{12}O_{40})_2\cdot 2H_2O]\cdot 4H_2O$ (2)

$NiSO_4$ (0.1 g, 0.38 mmol), $K_6Na_2[GeW_{11}O_{39}]\cdot 13H_2O$ (0.07 g, 0.023 mmol) and dm4bt (0.03 g, 0.15 mmol) were dissolved in 10 mL of distilled water at room temperature. The suspension was stirred for 30 min in air, and the pH of the solution was then adjusted to about 1.73 with 1.0 mol·L^{-1} HCL. The resulting suspension was sealed in a Teflon-lined autoclave (25 mL) and kept at 160 °C for 4 days. After cooling to room temperature, green block crystals of **2** (0.036 g, yield 45% based on W) were obtained and the final pH is 1.86. Anal. Calcd for **2** $C_{64}H_{76}Ni_4Ge_2N_{16}O_{86}S_{16}W_{24}$(7750): C 9.92, H 0.99, N 2.89%. Found: C 9.95, H 0.97, N 2.93%.

Synthesis of $[Co_4^{II}(dm4bt)_8(GeW_{12}O_{40})_2\cdot 2H_2O]\cdot 4H_2O$ (3)

The synthetic means of **3** are similar to **2**, except that use $CoSO_4$ (0.08 g, 0.285 mmol) instead of $NiSO_4$ and the pH value of about 2.03. After cooling to room temperature, orange-yellow block crystals of **3** (0.039 g, yield 50% based on W) were obtained and the final pH is 1.95. Anal. Calcd for **3** $C_{64}H_{76}Co_4Ge_2N_{16}O_{86}S_{16}W_{24}$(7751): C 9.92, H 0.99, N 2.89%. Found: C 9.96, H 0.94, N 2.96%.

Synthesis of $[Co^{II}_4(dm4bt)_8(SiW_{12}O_{40})_2\cdot 2H_2O]\cdot 6H_2O$ (4)

The synthetic means of **4** are similar to **3**, except that use $H_4[SiW_{12}O_{40}]\cdot 14H_2O$ (0.09 g, 0.029mmol) instead of $K_6Na_2[GeW_{11}O_{39}]\cdot 13H_2O$ and the pH value of about 2.7. After cooling to room temperature, orange-yellow block crystals of **4** (0.06 g, yield 55% based on W) were obtained and the final pH is 2.52. Anal. Calcd for **4**

$C_{64}H_{68}Co_4Si_2N_{16}O_{82}S_{16}W_{24}$(7590): C 10.13, H 0.90, N 2.95%. Found: C 10.18, H 0.92, N 2.91%.

Synthesis of $[Cu^{II}_2(H_2bdpm)(HBW_{12}O_{40})\cdot 2H_2O]\cdot H_2O$ (5)

$CuCl_2$ (0.085 g, 0.632 mmol), $K_8[BW_{11}O_{39}]\cdot 13H_2O$ (0.1 g, 0.031 mmol) and H_2bdpm (0.02 g, 0.025 mmol) were dissolved in 10 mL of distilled water at room temperature. The suspension was stirred for 30 min in air, and the pH of the solution was then adjusted to about 3.7 with 1.0 mol·L^{-1} HCL. The resulting suspension was sealed in a Teflon-lined autoclave (25 mL) and kept at 150 °C for 5 days. After cooling to room temperature, green block crystals of **5** (0.055 g, yield 50% based on W) were obtained and the final pH is 3.48. Anal. Calcd for **5** $C_{44}H_{63}Cu_2BN_{16}O_{43}W_{12}$(3848): C 13.73, H 1.65, N 5.82%. Found: C 13.72, H 1.63, N 5.85%.

Preparation of compounds bulk-modified CPEs

The carbon paste electrode of compound **1** (**1**–CPE) was made by the following method: a mixture of compound **1** (0.01 g) and 0.1 g of graphite powder was ground by using an agate mortar. And then 0.1 mL of liquid paraffin was added to the mixture with stirring. The mixture was then slowly place in a glass tube (with an inner diameter of 1.5mm), and the tube surface was wiped with weighing paper. Electrical contact was established by using a suitable copper rod through the back of the electrode. With the similar method, **2–** to **5–**CPEs were made by using compounds **2** to **5**.

The quenching efficiency of compounds for $Cr_2O_7^{2-}$

The Stern−Volmer (S−V) equation: $I_0/I = 1+K_{sv}[C]$

where I_0 and I are the luminescence intensities before and after the addition of $Cr_2O_7^{2-}$, respectively. K_{sv} is the Stern−Volmer quenching constant (M^{-1}), and [C] is the concentration of $Cr_2O_7^{2-}$.

The limit of detection (LOD) can be determined by the equation $LOD = 5\sigma/K_{sv}$, where σ is the standard deviation from five blank measurements and k is the slope of the calibration curve at lower concentrations.

Electroreduction CO_2 Measurement

The CO_2RR experiments were carried out by using an H-type glass cell in 0.5 M $KHCO_3$ solution under CO_2 and N_2 atmospheres (the H-type glass cell separated by Nafion 117 membrane). A Solarton workstation was used to record the electrochemical response and collect data. The working electrode was made by the following method: dispersing 5 mg compound **1** and 10 μl Nafion solution (5 wt%) in 490 μl ethanol solution to obtain catalytic ink (10 mg·ml^{-1}), which was loaded onto a dry carbon fiber paper at a temperature of 50 °C. During the reaction, N_2 and CO_2 are flushed into the glass cell at a rate of 20 mL/min, the gas products were measured using online gas chromatography. All measured potentials were obtained against the Ag/AgCl reference electrode and converted to the reversible hydrogen electrode (RHE scale) based on the Nernst equation:

$$E_{RHE} = E_{SCE} + 0.2415V + 0.0592V \times pH$$

For CO_2-saturated 0.5 M $KHCO_3$ (pH=7.3), N_2-saturated 0.5 M $KHCO_3$ (pH=8.6). According to the definition of Faradic efficiency [1], the faradaic efficiencies of the gas products were obtained:

$$FE_i = \frac{Z_i \times V_i \times G \times F \times P_0}{I \times R \times T_0 \times 60000}$$

i: CO, H_2;

Z_i: number of electrons required to produce an i molecule, which is 2, 2 for CO and H_2;

V_i: volume of the GC sampling loop;

G: the volumetric flow rate;

F: Faradaic constant (96485.33289 C mol^{-1});

P_0: atmospheric pressure (1.013×10^5Pa);

I: the average current in a period (t) of electrocatalysis;

T_0: reaction temperature (298 K);

R: ideal gas constant (8.314 J mol^{-1} K^{-1}).

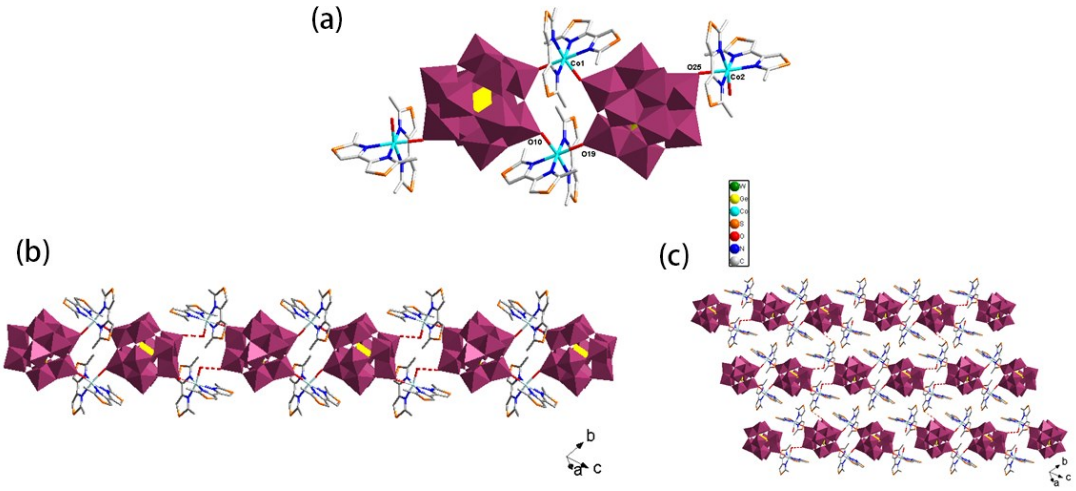

Figure S1. (a) Stick/polyhedral view of the symmetric unit of **3**. The hydrogen atoms and crystal water molecules are omitted for clarity. (b) and (c) The 1D supramolecular chain and 2D supramolecular layer through hydrogen bonds.

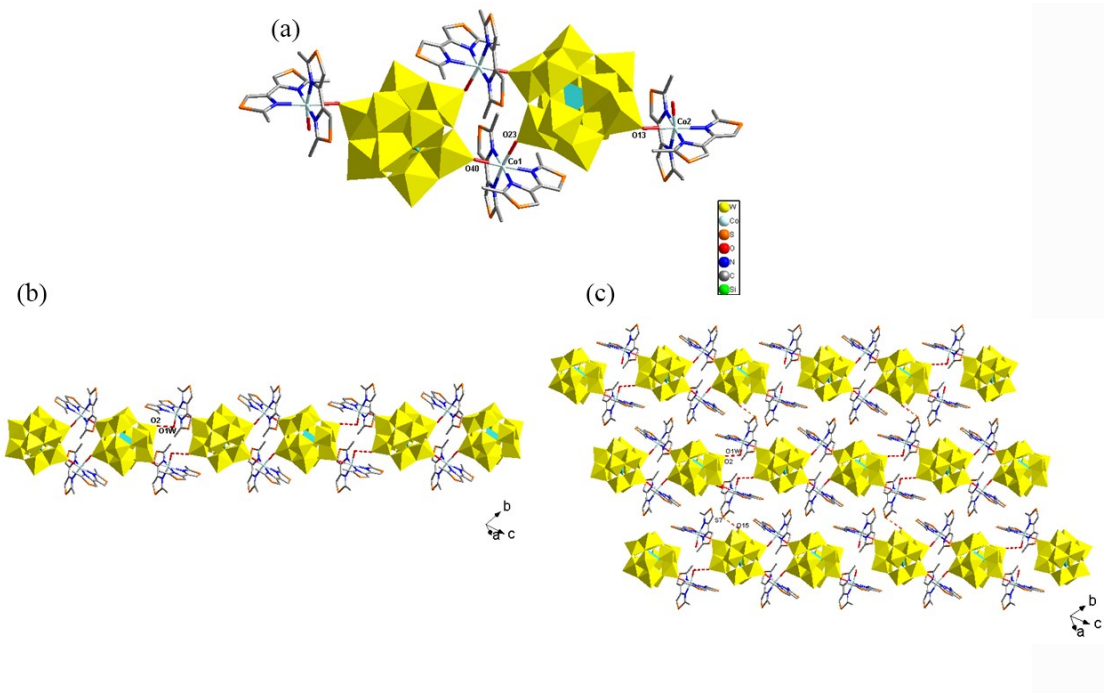

Figure S2. (a) Stick/polyhedral view of the symmetric unit of **4**. The hydrogen atoms and crystal water molecules are omitted for clarity. (b) and (c) The 1D supramolecular chain and 2D supramolecular layer through hydrogen bonds.

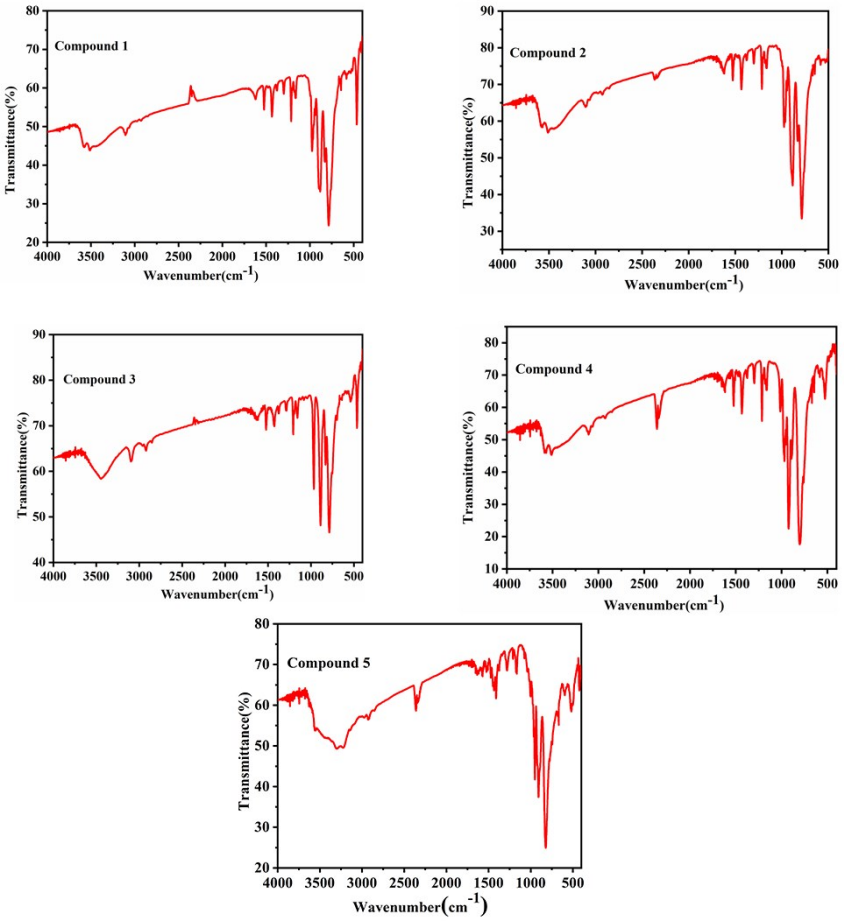

Figure S3. The IR spectra of compounds **1**–**5**.

In the FT-IR spectra, the characteristic peaks at 976, 882, 785 cm^{-1} for **1**, 975, 883, 784 cm^{-1} for **2**, 966, 888, 787 cm^{-1} for **3** are attributed to ν (W-O_d), ν (W-O_b-W), and ν(W-O_c-W) of GeW_{12} polyoxoanion. The characteristic peaks at 1015, 969, 924, 801 cm^{-1} for **4** are attributed to ν(Si-O_a), ν(W-O_t), ν(W-$O_{b/c}$-W) of SiW_{12} polyoxoanion. The characteristic peaks at 950, 907, 820 cm^{-1} for **5** are attributed to ν(B-O_a), ν(W-O_t), ν(W-$O_{b/c}$-W) of BW_{12} polyoxoanion, respectively [2-4]. The characteristic peaks in the region of 1623–1160 cm^{-1} for **1**, 1617–1165 cm^{-1} for **2**, 1618–1158 cm^{-1} for **3**, 1624–1161 cm^{-1} for **4**, 1653–1165 cm^{-1} for **5**, are attributed to dm4bt in **1**, **2**, **3** and **4** and H_2bdpm in **5**, respectively[5-6].

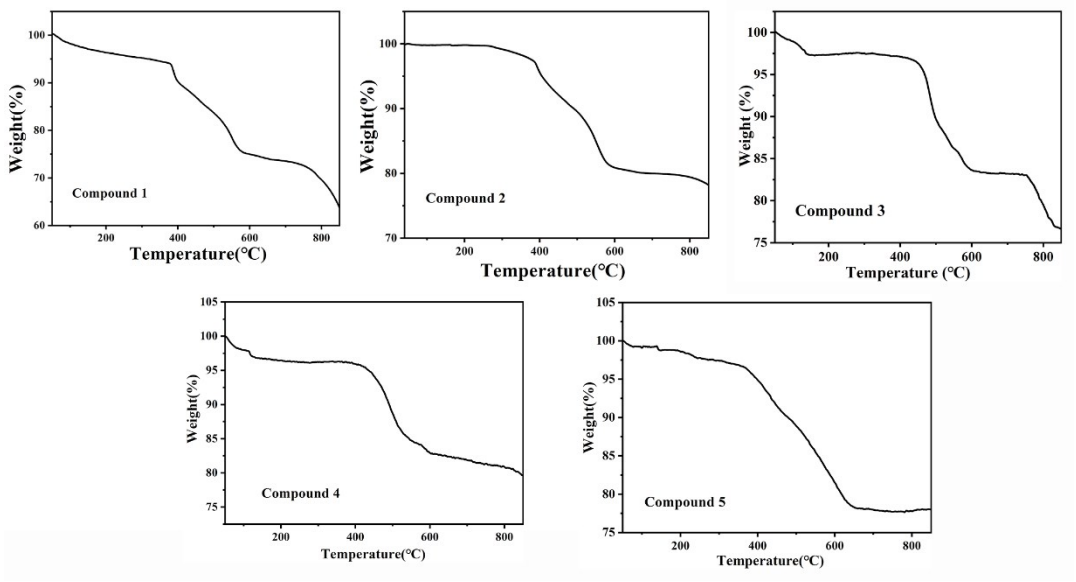

Figure S4. The TG curves of compounds **1**–**5**.

TG-DTA analyses of compounds **1**–**5** were tested in the range of 50–850°C under N_2 atmosphere with a heating rate of 10 $^oC \cdot min^{-1}$. The results of thermogravimetric analysis show that the title compounds have two main steps of weight loss: the first step weight loss below 300 ^oC is attributed to the loss of water molecules, and the second step mass loss in the range of 400–850^oC is attributed to the loss of organic ligands. In the range of 50 to 850^oC, the total weight loss of these five compounds is in good agreement with the calculated value, namely, 36.2% for compound **1** (calculated value: 35.5%), 21.8% for compound **2** (calculated value: 21.6%), 22.3% for compound **3** (calculated value: 21.6%), 20.4% for compound **4** (calculated value: 21.2%), 22.1% for compound **5** (calculated value: 22.7%).

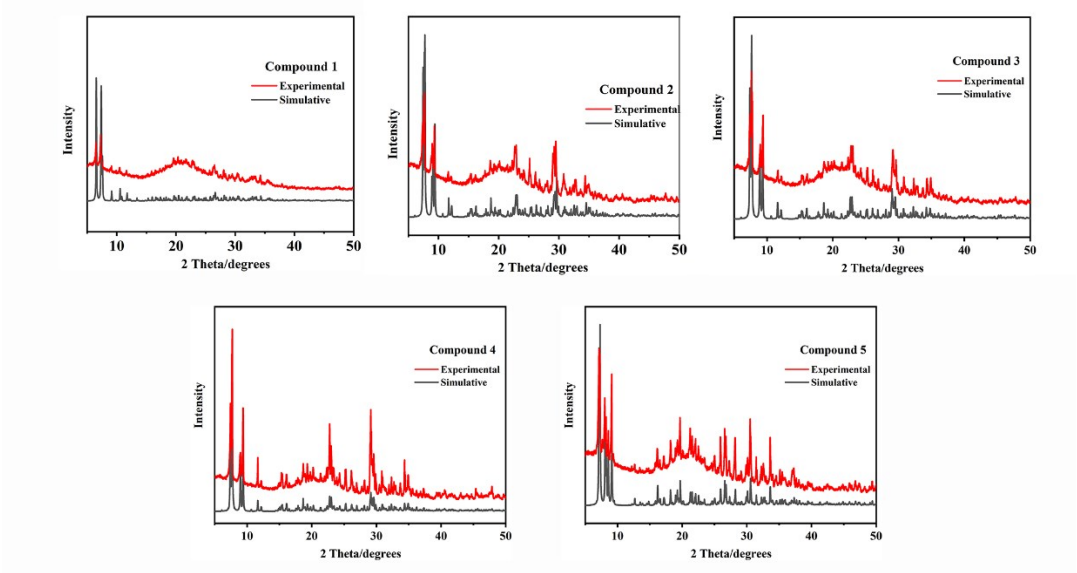

Figure S5. The simulative (black line) and experimental (red line) powder X-ray diffraction patterns for compounds **1**–**5**.

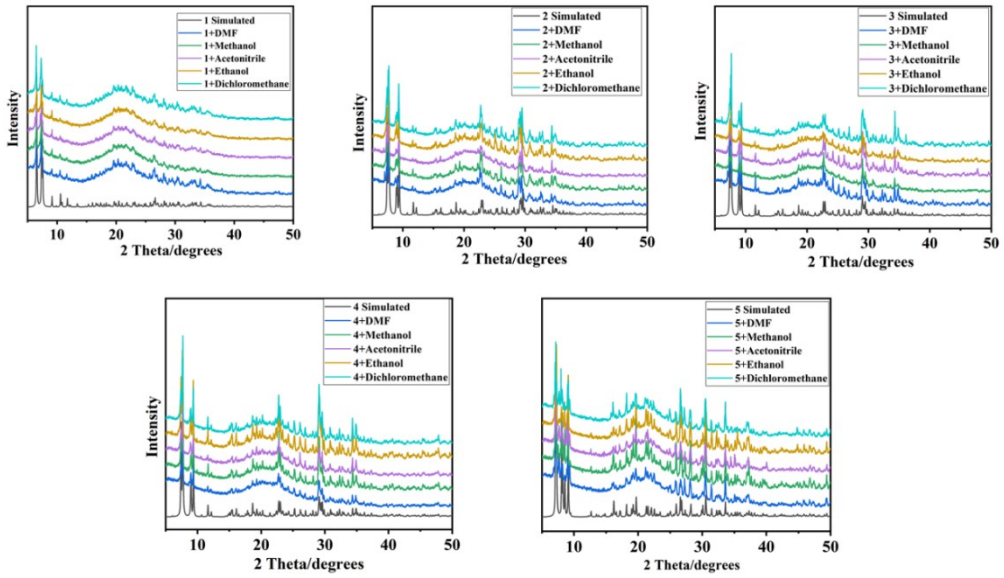

Figure S6. The PXRD of compounds **1**–**5** after immersed in different organic solvents.

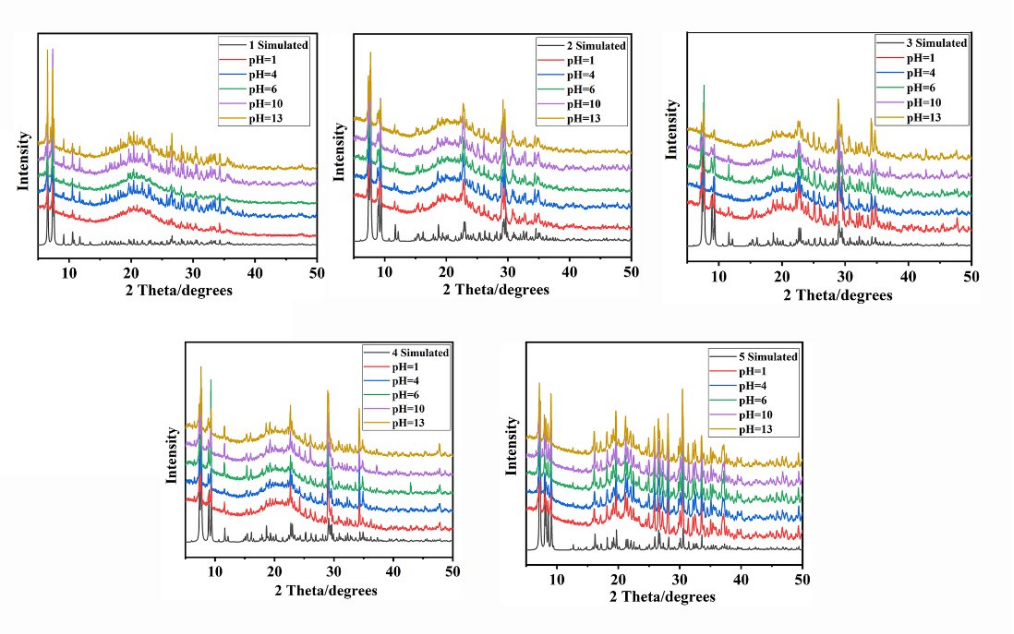

Figure S7. The PXRD of compounds **1**–**5** after immersed in aqueous solutions with different pH values.

The crystal purity of compounds **1**–**5** can be verified through using Powder X-ray diffraction**.** It can be seen from the PXRD graph that compounds **1**–**5** have higher purity (Figure S5). Furthermore, we studied the stability of compounds **1**–**5** by immersing compounds **1**–**5** in different organic solvents (DMF, methanol, acetonitrile, ethanol and dichloromethane) and aqueous solutions with different pH values (pH = 1, 4, 6, 10 and 13) for 24 hours. The simulated and experimental diffraction peaks match well in positions, which shows that the structure of these compounds has not changed and compounds **1**–**5** have excellent stability (Figure S6-S7).

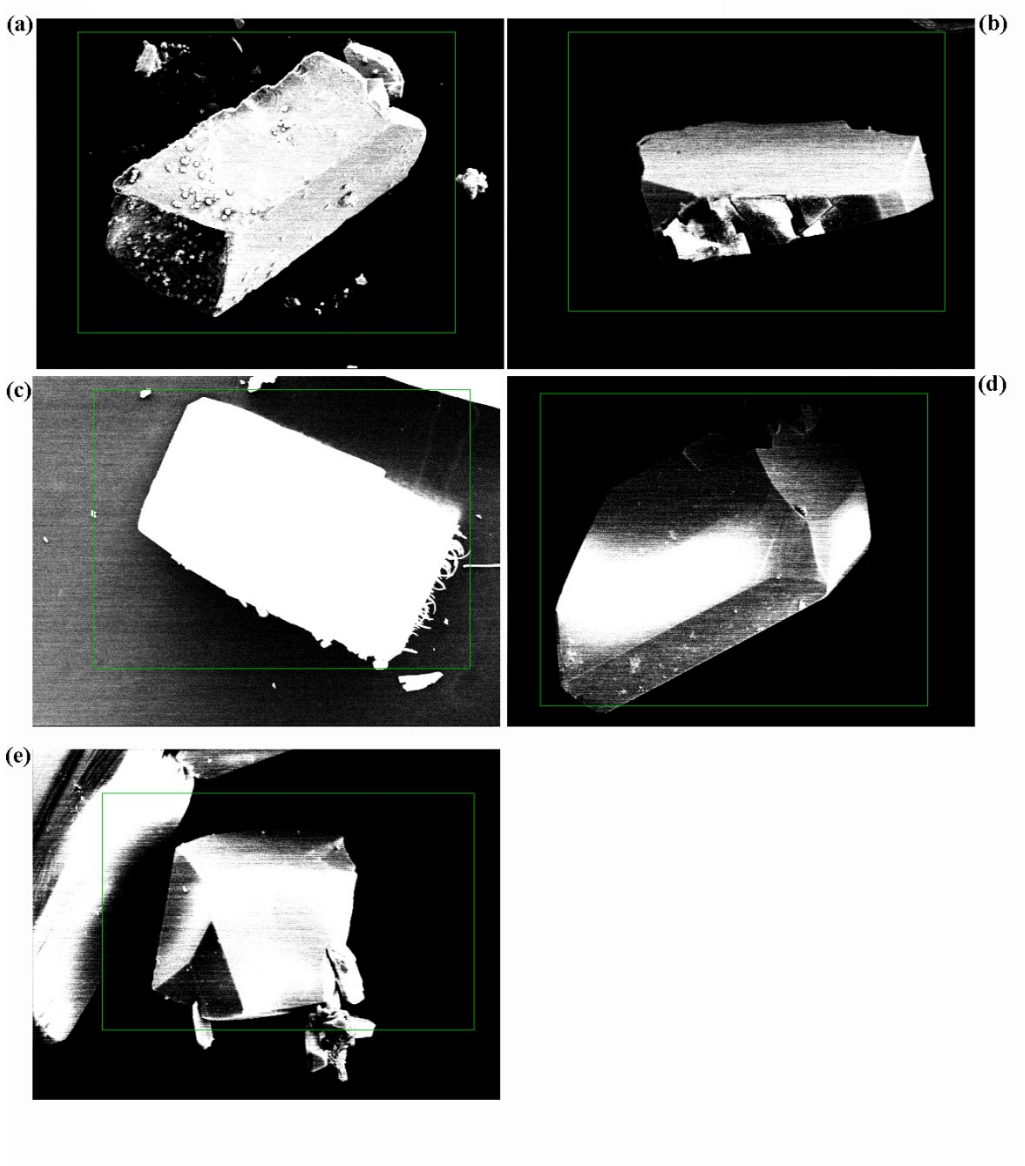

Figure S8. The SEM of compounds **1**–**5** (a-e).

The morphology of the as-synthesized POM-based compounds was characterized by scanning electron microscopy. As shown in Figure S8, POM-based crystals have block shapes.

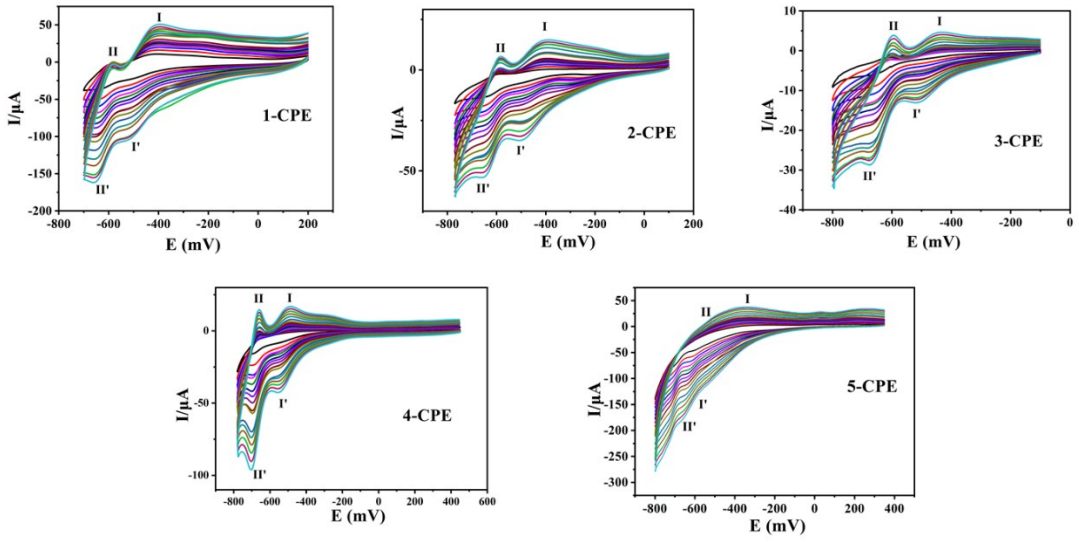

Figure S9. The cyclic voltammograms of the **1–** to **5**−CPEs in 0.1M H_2SO_4 + 0.5M Na_2SO_4 aqueous solution at different scan rates (from inner to outer: 20, 40, 60, 80, 100, 120, 140, 160, 180, 200, 250, 300, 350, 400, 450 and 500 mVs^{-1}, respectively).

Herein, we used the title compounds to make carbon paste electrodes, and electrochemical workstation was used to study the electrochemical properties of compounds **1**–**5** through three electrode system in electrolyte solution (0.1 M H_2SO_4 + 0.5 M Na_2SO_4 aqueous solutions). The cyclic voltammogram for **1–** to **5**−CPEs at different scan rates are shown in Figure S8. For **1–**, **2–** and **3–**CPEs, two pairs reversible redox peaks I-I' and II-II' are observed, which belong to two electron transfer processes of GeW_{12} anion [2]. For **4–**CPE, there are two pairs reversible redox peaks I-I' and II-II', which belong to two electron transfer processes of SiW_{12} anion [7]. For **5–**CPE, there are two pairs reversible redox peaks I-I' and II-II', which belong to two electron transfer processes of BW_{12} anion [8]. The half-wave potentials, defined as $E_{1/2} = (E_{pa} + E_{pc})/2$, are -459(I-I') and -620(II-II') for **1–**CPE, -450(I-I'), -617(II-II') for **2–**CPE, -482(I-I'), -637(II-II') for **3–**CPE, -512(I-I'), -680 (II-II') for **4–**CPE, -435(I-I'), -630(II-II') for **5–**CPE (scan rate: 200 m $V \cdot s^{-1}$), respectively.

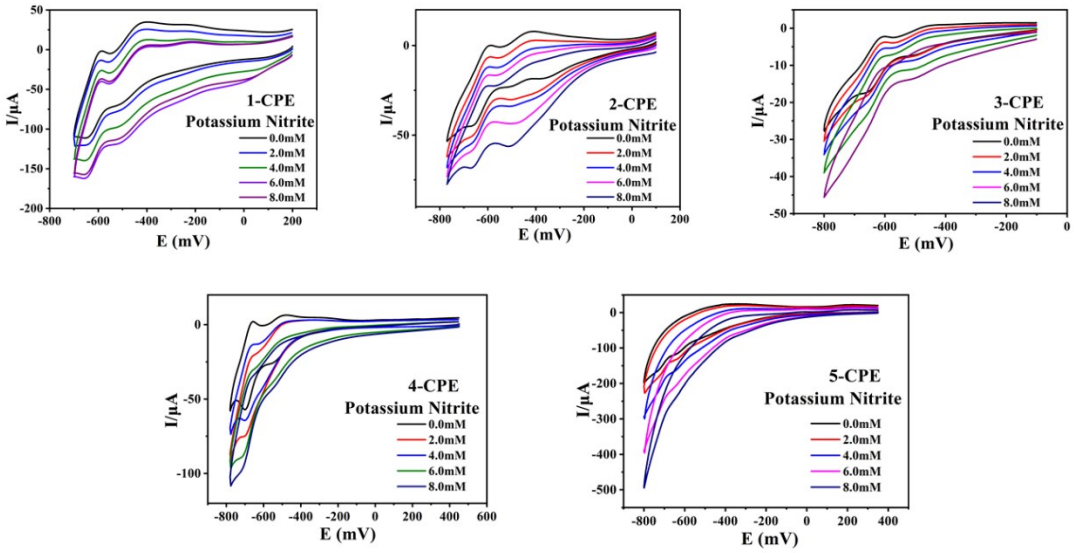

Figure S10. Cyclic voltammograms of the **1–** to **5**–CPEs in 0.1 M H_2SO_4 + 0.5 M Na_2SO_4 aqueous solution containing 0 (a); 2 (b); 4 (c); 6 (d) and 8 (e) mM KNO_2. Scan rate: 200 $mV \cdot s^{-1}$.

The electrocatalytic properties of compounds **1**–**5** were studied. 2.0 mM KNO_2 solution were continuously added to the electrolyte solution [9-10]. It can be clearly seen that by continuously adding KNO_2, both redox peaks I-I' and II-II' at **1**– to **5**–CPEs are catalytic peaks with the reduction peak current increasing and the oxidation peak current decreasing. The results exhibit that title compounds **1**–**5** are suitable to be used as electrode materials for dual-functional electrocatalysis for reduction of KNO_2.

In this part, the possible mechanism of electrochemical catalytic can be divided into two parts: the electrochemical reactions and chemical catalysis. In the part of electrochemical reaction, the process can be described by the following equations:

$$XW_{12}{}^{VI}O_{40}{}^{n-} + 2H^+ + 2e^- \leftrightharpoons H_2XW_{10}{}^{VI}W_2{}^{V}O_{40}{}^{n-} \text{ (I)}$$

$$H_2XW_{10}{}^{VI}W_2{}^{V}O_{40}{}^{n-} + 2H^+ + 2e^- \leftrightharpoons H_4XW_8{}^{VI}W_4{}^{V}O_{40}{}^{n-} \text{ (II)}$$

$$H_4XW_8{}^{VI}W_4{}^{V}O_{40}{}^{n-} + 2H^+ + 2e^- \leftrightharpoons H_6XW_4{}^{VI}W_6{}^{V}O_{40}{}^{n-} \text{ (III)}$$

In the part of chemical catalysis, the step can be described as following:

$$H_6XW_4{}^{VI}W_6{}^{V}O_{40}{}^{n-} + 6NO_2{}^- + 6H^+ \leftrightharpoons XW_{12}{}^{VI}O_{40}{}^{n-} + 6NO + 6H_2O \text{ (III)}$$

(X = Ge or Si, n=4; X= B, n=5)

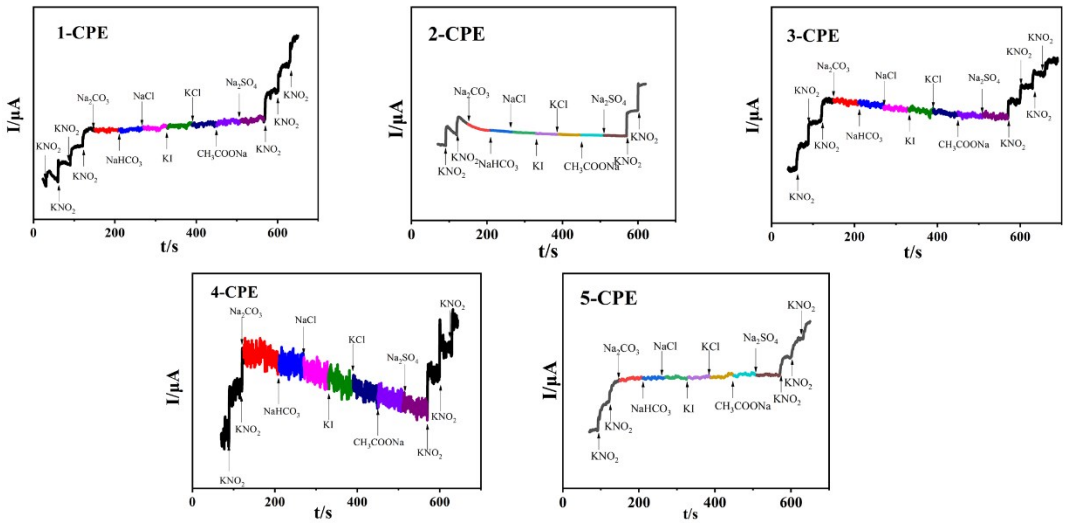

Figure S11. The anti-interference performance of the n–CPEs to KNO_2 and other metal ions in 0.1 M H_2SO_4 + 0.5 M Na_2SO_4 electrolyte.

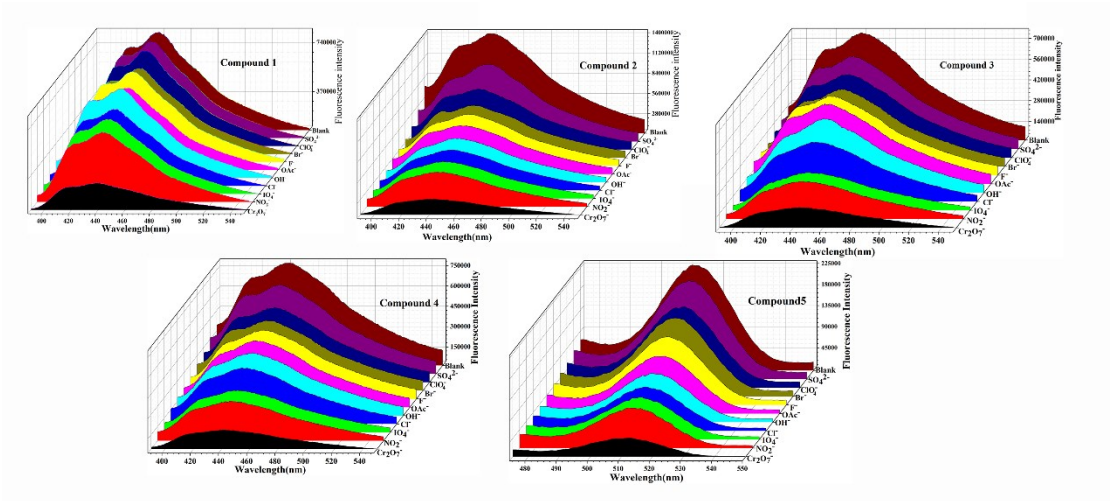

Figure S12. Fluorescence intensity of **1–5** suspension with the addition of different metal ions (excited at 365 nm for **1–4**, 254 nm for **5**).

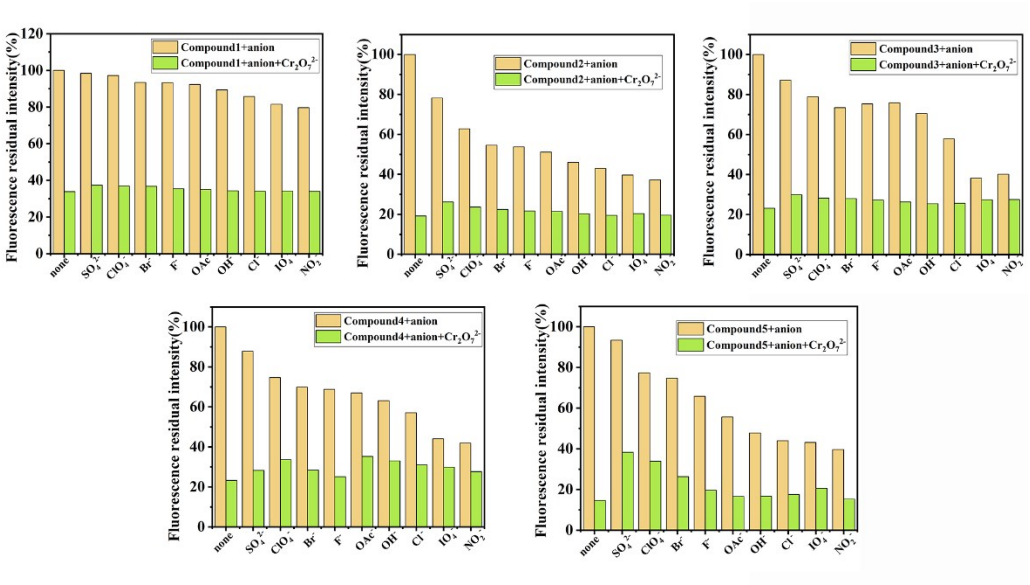

Figure S13. Bar diagram to show relative fluorescence intensity of compounds **1–5** in DMSO suspension upon addition of different anions and $Cr_2O_7^{2-}$ ions in equal concentration.

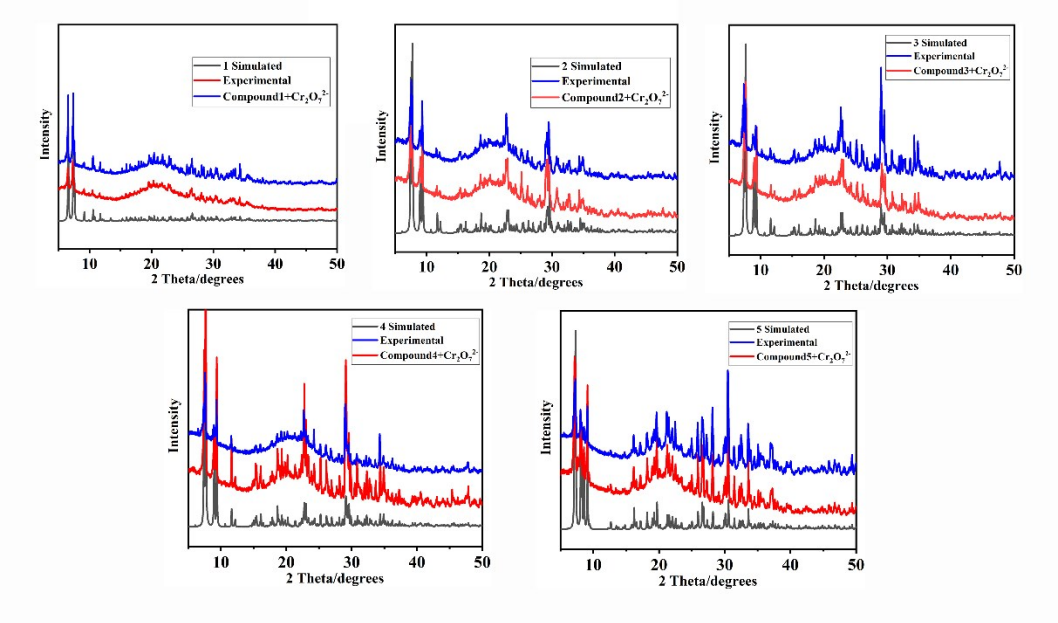

Figure S14. The simulative (black line), experimental (red line) and treated after fluorescence for $Cr_2O_7^{2-}$ solution (blue line) powder X-ray diffraction patterns for compounds **1**–**5**.

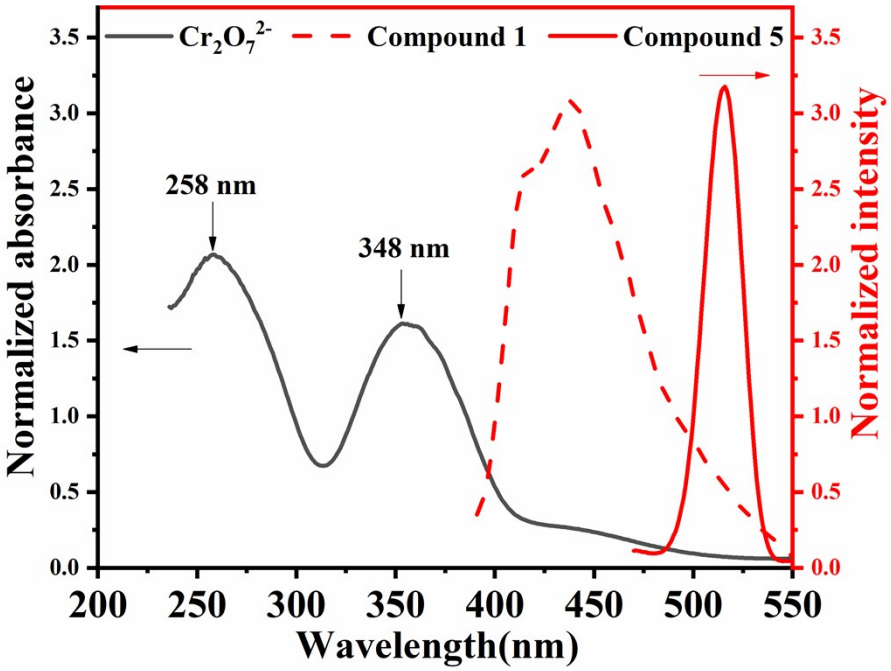

Figure S15. Spectral overlap between the UV-Vis absorption spectra of $Cr_2O_7^{2-}$ in H_2O and the emission spectra of compound **1** and **5** in DMSO suspensions.

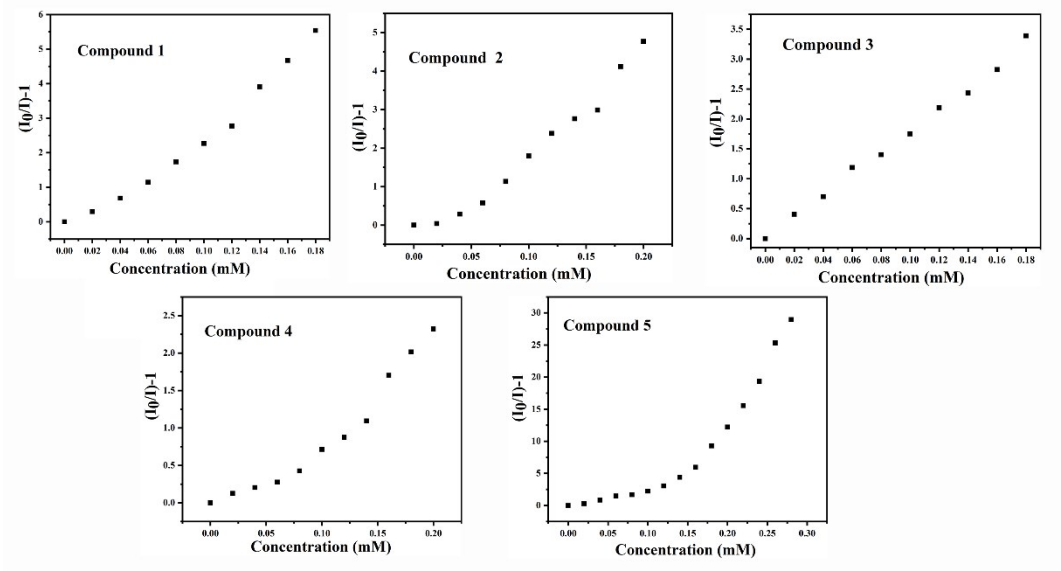

Figure S16. S-V plots for compounds **1–5** in DMSO suspension upon incremental addition of $Cr_2O_7^{2-}$.

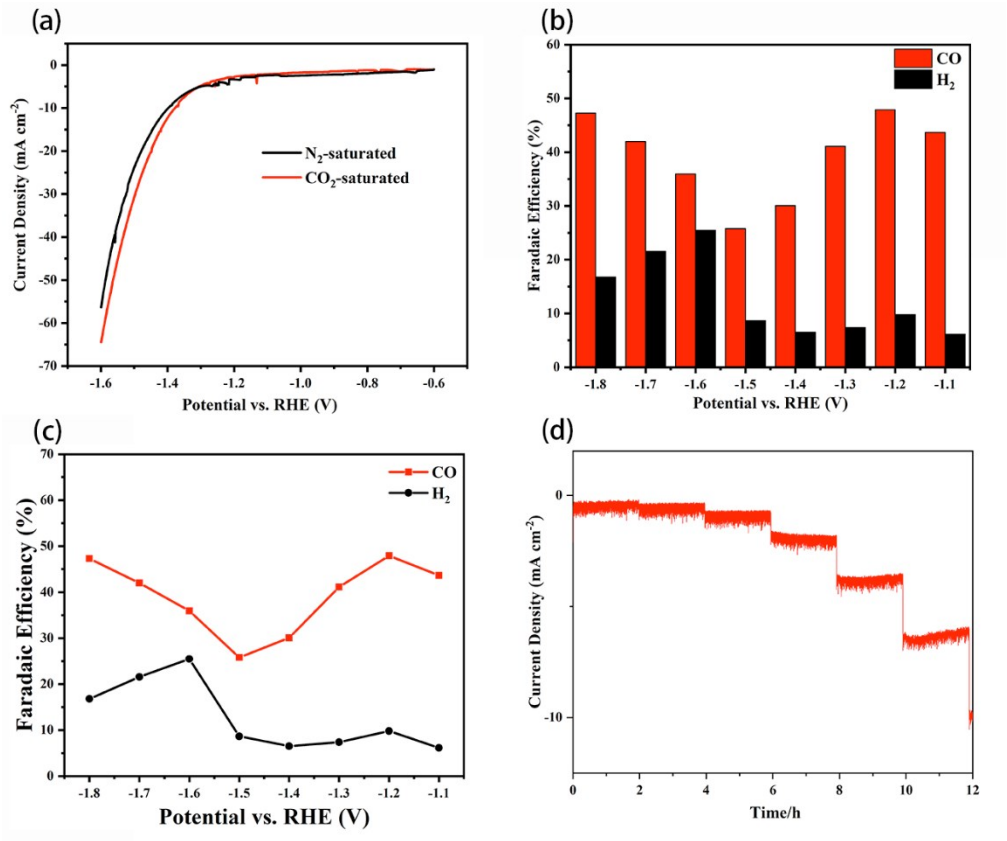

Figure S17. (a) LSV curves of compound **1** in CO_2-saturated and N_2-saturated 0.5 M $KHCO_3$ electrolyte on carbon paper at a scan rate of 5 mV s^{-1}. (b) The Faradaic efficiency of compound **1** for CO (red bars) and H_2 (black bars). (c) The FE of CO and H_2 products on compound **1** at selected potentials. (d) The Current density v.s. time curve of compound **1** during the electrolysis.

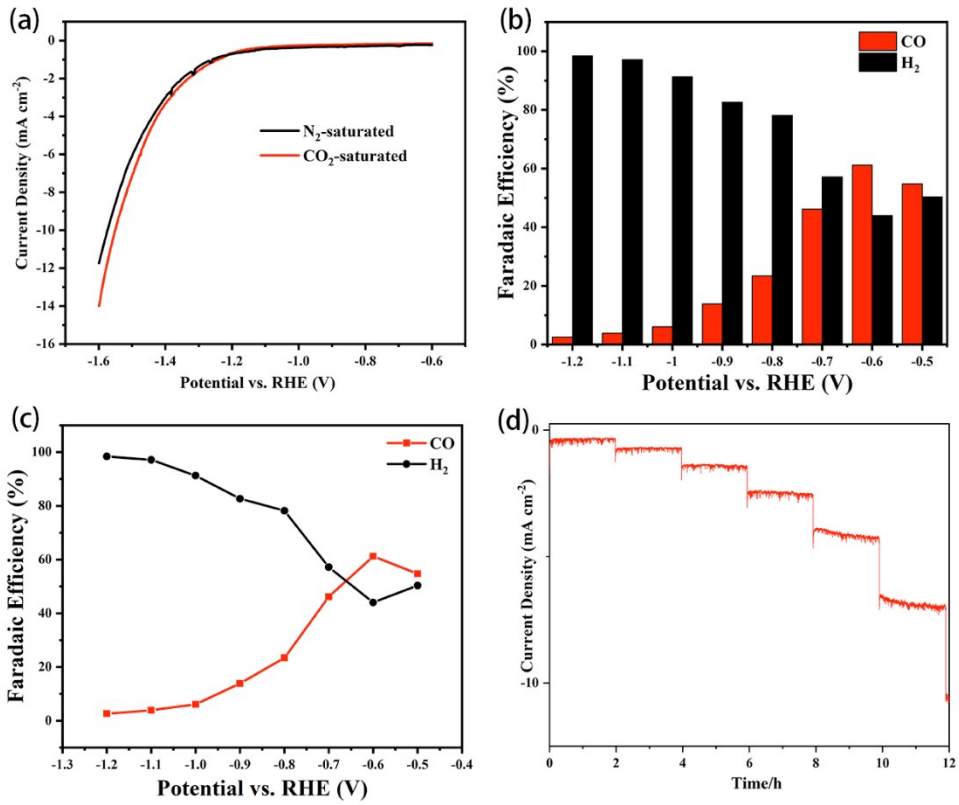

Figure S18. (a) LSV curves of compound **3** in CO_2-saturated and N_2-saturated 0.5 M $KHCO_3$ electrolyte on carbon paper at a scan rate of 5 mV s^{-1}. (b) The Faradaic efficiency of compound **3** for CO (red bars) and H_2 (black bars). (c) The FE of CO and H_2 products on compound **3** at selected potentials. (d) The Current density v.s. time curve of compound **3** during the electrolysis.

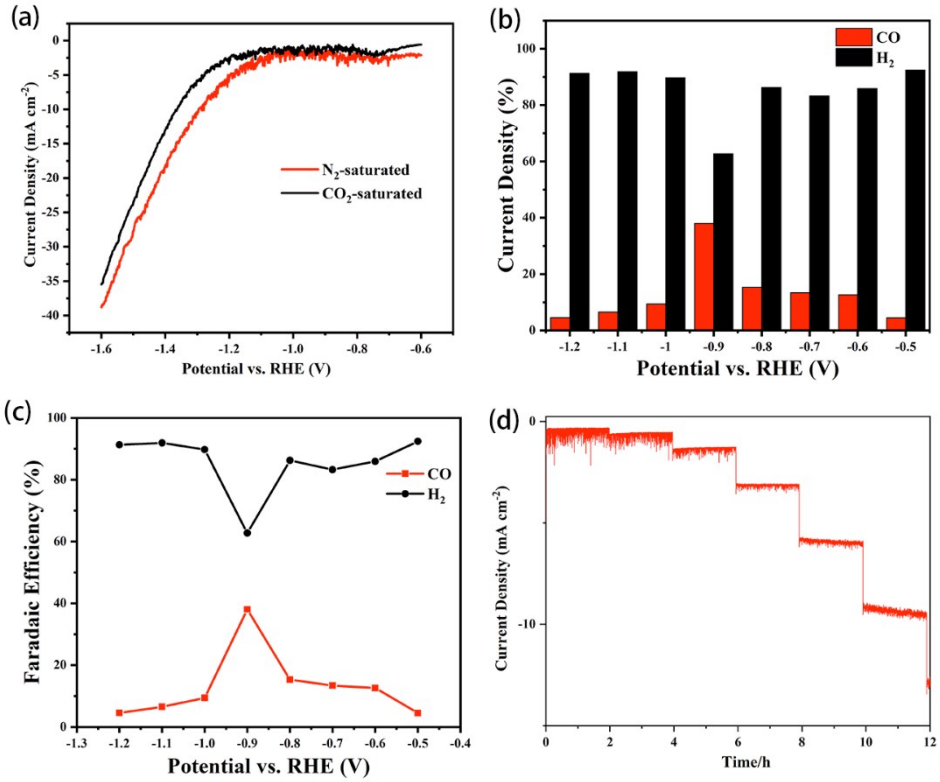

Figure S19. (a) LSV curves of compound **4** in CO_2-saturated and N_2-saturated 0.5 M $KHCO_3$ electrolyte on carbon paper at a scan rate of 5 mV s^{-1}. (b) The Faradaic efficiency of compound **4** for CO (red bars) and H_2 (black bars). (c) The FE of CO and H_2 products on compound **4** at selected potentials. (d) The Current density v.s. time curve of compound **4** during the electrolysis.

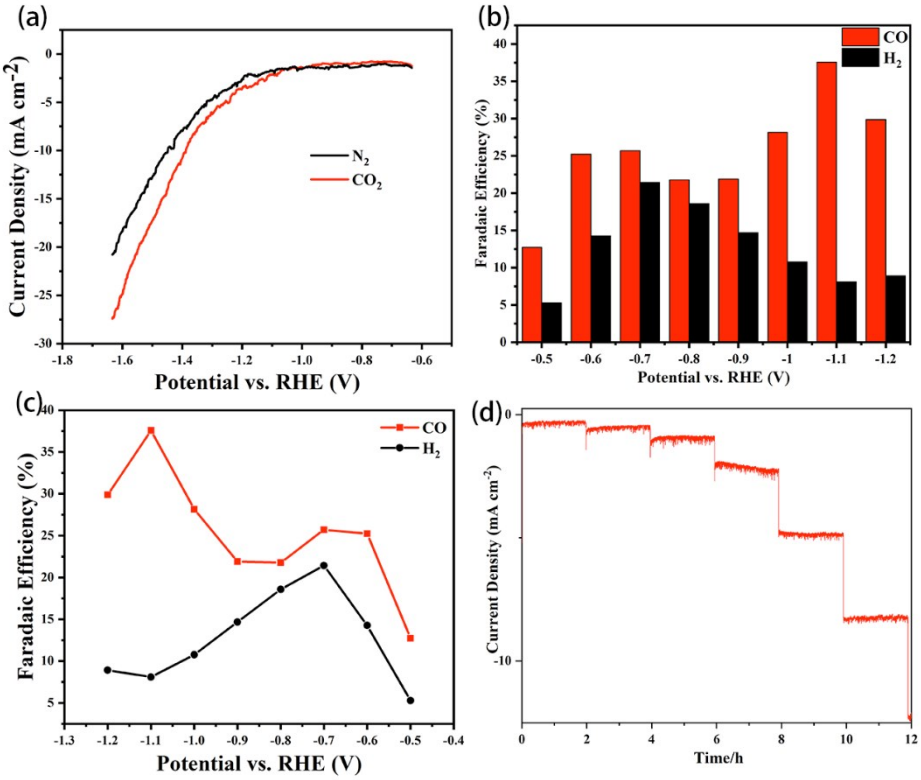

Figure S20. (a) LSV curves of compound **5** in CO_2-saturated and N_2-saturated 0.5 M $KHCO_3$ electrolyte on carbon paper at a scan rate of 5 mV s^{-1}. (b) The Faradaic efficiency of compound **5** for CO (red bars) and H_2 (black bars). (c) The FE of CO and H_2 products on compound **5** at selected potentials. (d) The Current density v.s. time curve of compound **5** during the electrolysis.

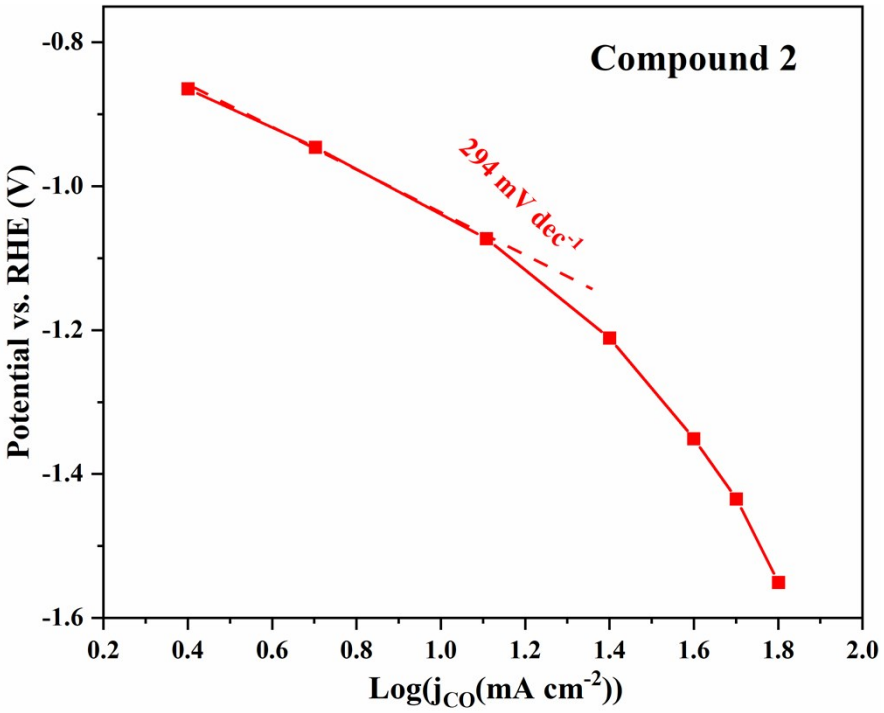

Figure S21. The Tafel plot of compound **2**.

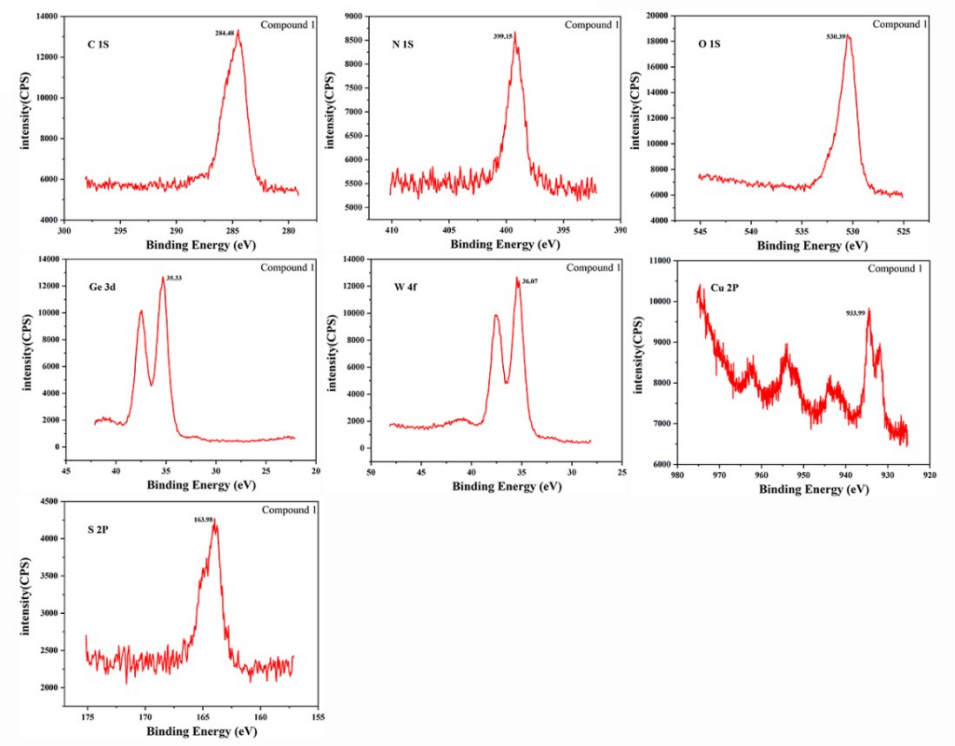

Figure S22. The X-Ray photoelectron spectroscopy of compound **1** after electrocatalysis.

Meanwhile, the XPS measurement for compounds indicates that all compounds are stable in the process of electrocatalysis.

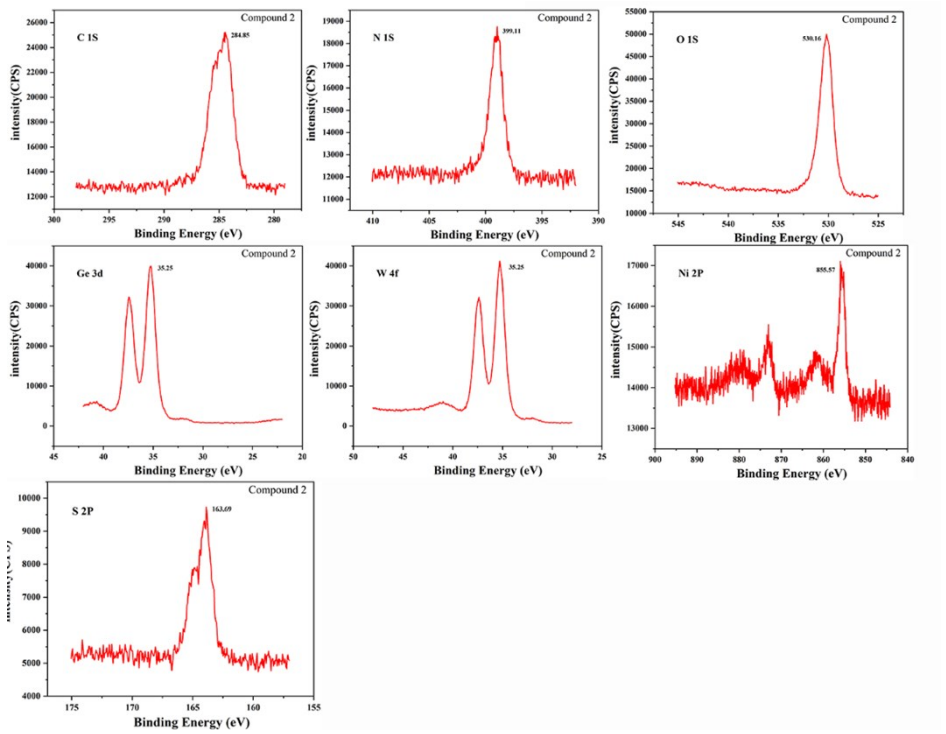

Figure S23. The X-Ray photoelectron spectroscopy of compound **2** after electrocatalysis.

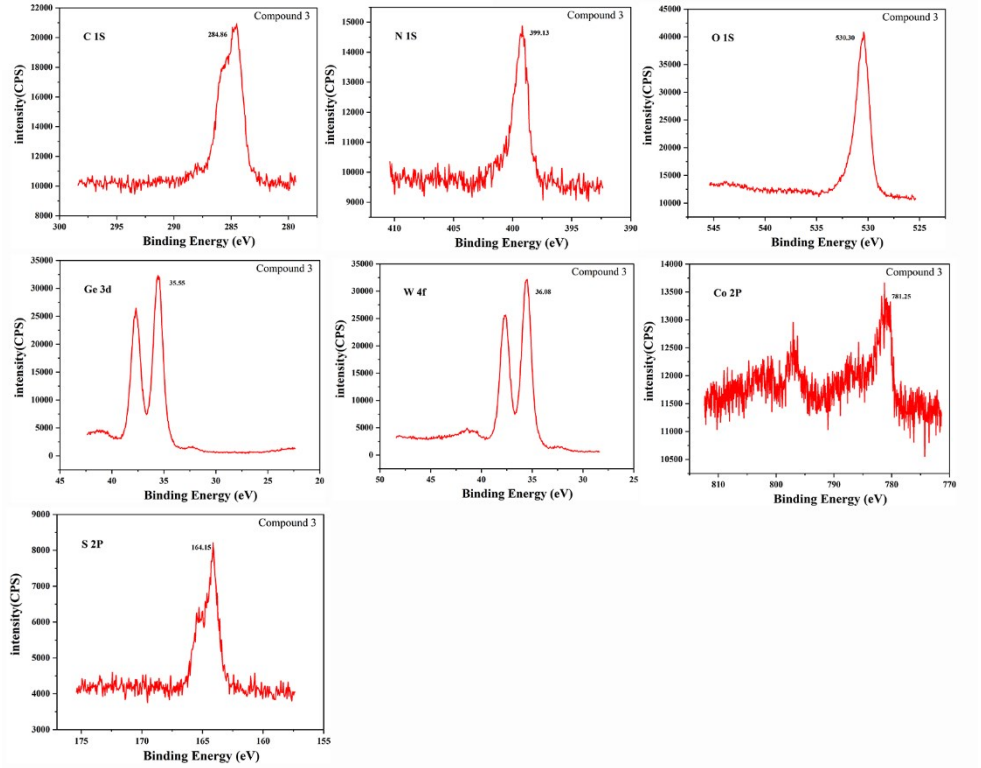

Figure S24. The X-Ray photoelectron spectroscopy of compound **3** after electrocatalysis.

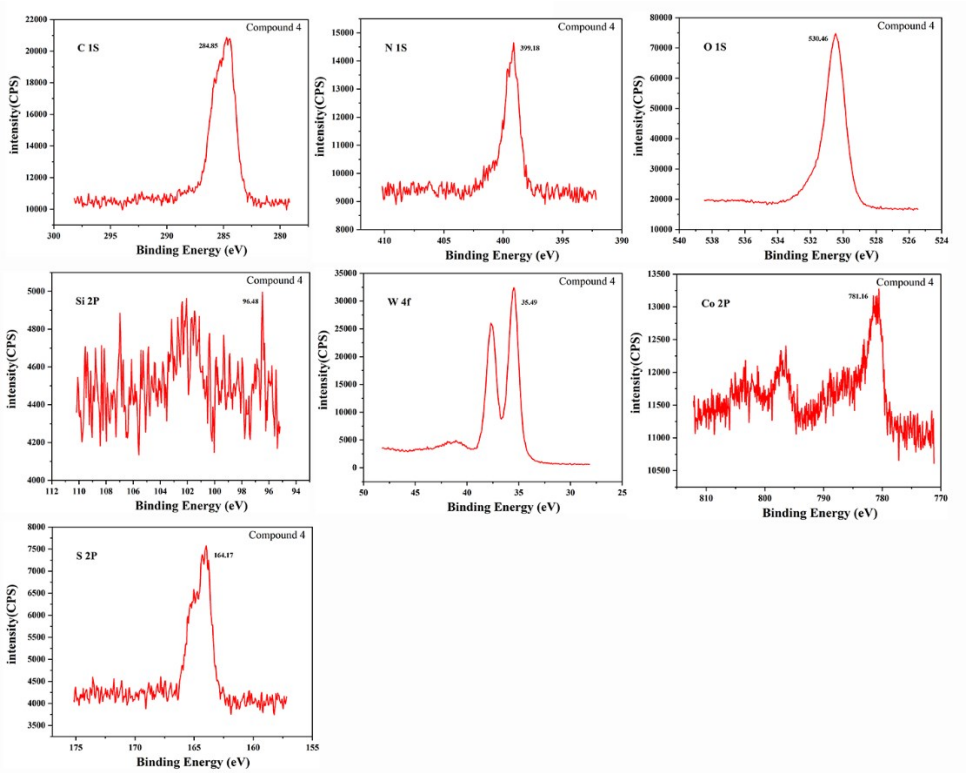

Figure S25. The X-Ray photoelectron spectroscopy of compound **4** after electrocatalysis.

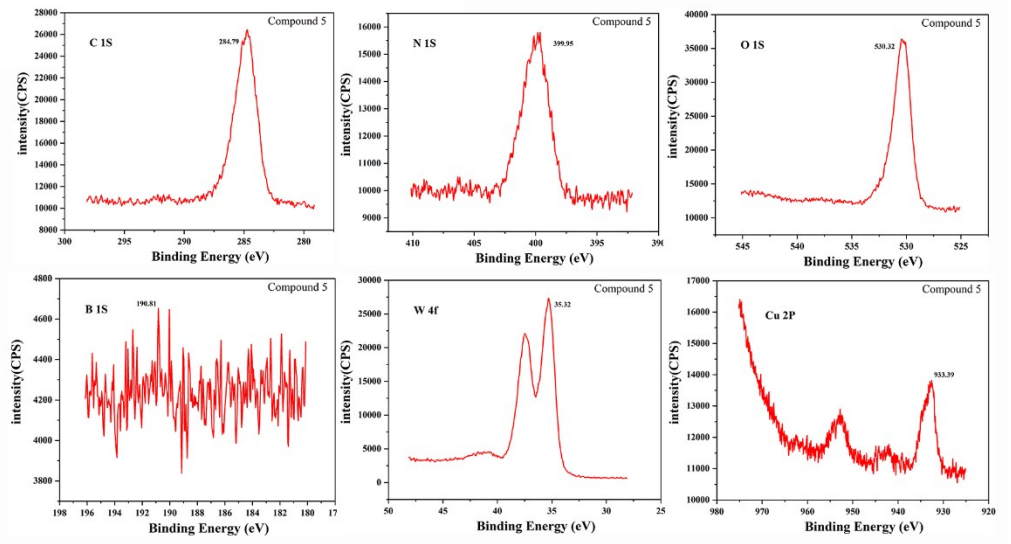

Figure S26. The X-Ray photoelectron spectroscopy of compound **5** after electrocatalysis.

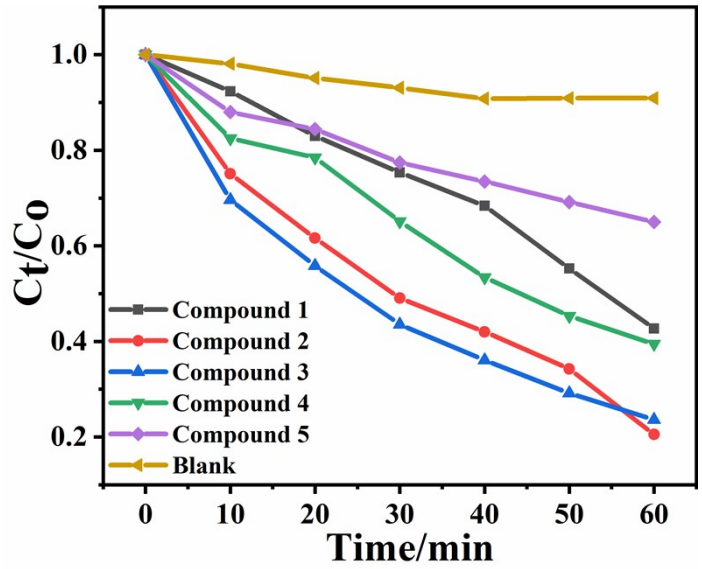

Figure S27. The catalytic conversion curve of compound **1**–**5** and blank experiment for Cr(VI) solution.

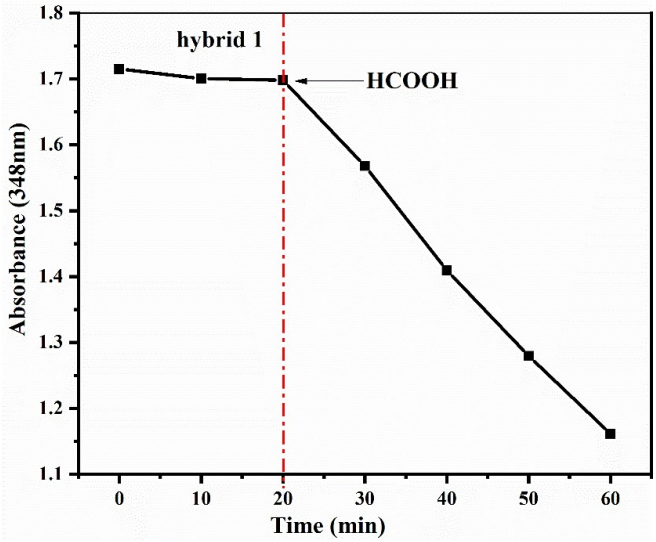

Figure S28. A comparative experiment for the reduction of Cr(VI) catalyzed by hybrid **1** at 50 °C: FA-free solution in the first 20 min; adding FA into the solution to run the reduction reaction.

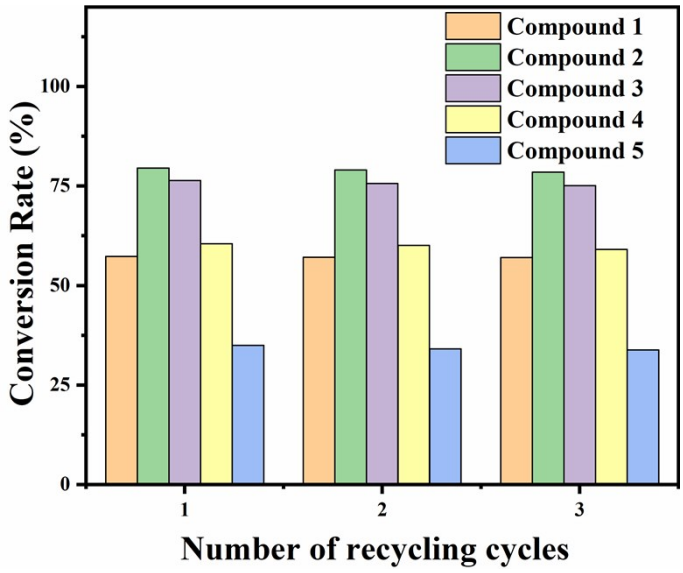

Figure S29. 3th cycles for the catalytic reduction of Cr(VI) with compounds **1**–**5**.

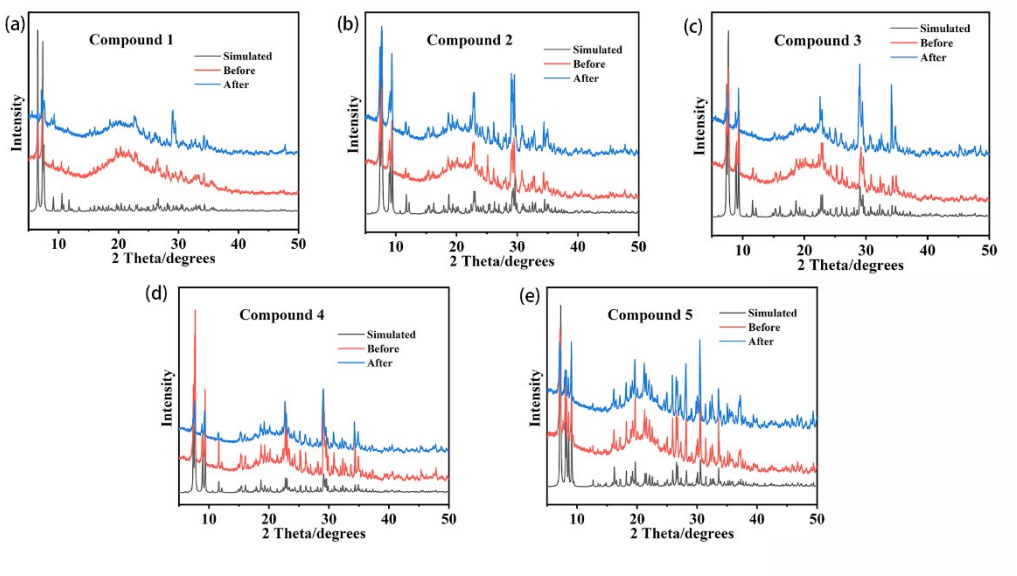

Figure S30. The simulative (black line), experimental (red line) and after catalytic reduction for Cr(VI) (blue line) powder X-ray diffraction patterns of compounds **1**–**5**.

Table S1. Crystal data and structure refinements for compounds **1**–**5**.

	1	**2**	**3**	**4**	**5**
Formula	$C_{64}H_{64}Cu_4GeN_{16}O_{40}S_{16}W_{12}$	$C_{64}H_{76}Ni_4Ge_2N_{16}O_{86}S_{16}W_{24}$	$C_{64}H_{76}Co_4Ge_2N_{16}O_{86}S_{16}W_{24}$	$C_{64}H_{68}Co_4Si_2N_{16}O_{82}S_{16}W_{24}$	$C_{44}H_{63}Cu_2BN_{16}O_{43}W_{12}$
*F*w	4743.16	7750.51	7751.47	7590.37	3848.09
crystal system	monoclinic	Triclinic	Triclinic	Triclinic	monoclinic
space group	P 21/n	P -1	P -1	P -1	-C 2yc
a (Å)	14.0266(10)	12.315(3)	12.374(3)	12.3151(19)	24.4397(7)
b (Å)	24.0079(16)	15.474(4)	15.539(4)	15.487(2)	14.9911(7)
c (Å)	16.5999(12)	19.504(5)	19.761(5)	19.695(3)	23.8988(9)
α (°)	90	86.664(5)	86.897(5)	86.760(4)	90
β (°)	100.791(2)	87.320(5)	87.383(5)	87.368(4)	116.637(1)
γ (°)	90	69.631(5)	69.637(5)	69.774(3)	90
V (Å^3)	5491.2(7)	3477.0(15)	3555.5(16)	3517.7(9)	7826.7(5)
Z	2	1	1	1	4
D_c (g·cm^{-3})	2.907	3.701	3.620	3.583	3.265
μ (mm^{-1})	13.925	21.048	20.520	20.335	18.185
F(000)	4408.0	3468.0	3464.0	3388.0	6932.0
R_1[a] [I > 2σ(I)]	0.0737	0.0569	0.0498	0.0707	0.0257
wR_2[b] (all data)	0.1849	0.1286	0.1084	0.1806	0.054
GOF on F^2	1.009	0.967	0.958	0.924	1.031

[a] $R_1=\sum \| F_o \| - | F_c \| / \sum | F_o |$. [b] $wR_2 = \{\sum[w(F_o^2-F_c^2)^2]/\sum[w(F_o^2)^2]\}^{1/2}$

Table S2. Selected bond distances (Å) and angles (°) for compounds **1**–**5**.

Compound **1**

Cu(1)-N(1)	1.98(2)	Cu(1)-N(2)	2.06(3)
Co(1)-N(3)	2.03(2)	Cu(1)-N(4)	2.07(3)
Cu(2)-N(5)	1.98(3)	Cu(2)-N(6)	2.22(2)
Cu(2)-N(7)	2.11(2)	Cu(2)-N(8)	2.05(3)
N(1)-C(2)	1.35(4)	N(2)-C(5)	1.45(4)
S(3)-C(10)	1.73(4)	S(2)-C(6)	1.71(3)
N(2)-C(5)	1.45(4)	N(3)-C(12)	1.39(4)
N(2)-Cu(1)-N(4)	99.4(10)	N(3)-Cu(1)-N(2)	129.1(9)
N(3)-Cu(1)-N(4)	83.3(11)	N(1)-Cu(1)-N(2)	80.6(9)
N(1)-Cu(1)-N(3)	129.7 (10)	N(1)-Cu(1)-N(4)	137.2(10)

N(5)-Cu(2)-N(6)	81.2(10)	N(5)-Cu(2)-N(8)	151.0(10)
N(5)-Cu(2)-N(7)	124.3(10)	N(8)-Cu(2)-N(6)	102.4(8)
N(8)-Cu(2)-N(7)	81.7(10)	N(7)-Cu(2)-N(6)	110.9(8)
C(23)-N(5)-Cu(2)	130(2)	C(20)-N(5)-Cu(2)	114(2)

Compound **2**

Ni(1)-N(1)	2.098(16)	Ni(1)-N(2)	2.103(14)
Ni(1)-N(3)	2.043(15)	Ni(1)-N(4)	2.129(16)
Ni(1)-O(39)	2.126(12)	Ni(1)-O1W	2.102(12)
Ni(2)-N(5)	2.084(15)	Ni(2)-N(6)	2.146(17)
Ni(2)-N(7)	2.077(14)	Ni(2)-N(8)	2.054(14)
Ni(2)-O(40)	2.083(11)	Ni(2)-O(8)#1	2.252(12)
S(7)-C(26)	1.728(17)	S(1)-C(6)	1.68(2)
N(2)-Ni(1)-O(39)	173.6(5)	N(2)-Ni(1)-N(4)	100.3(6)
N(3)-Ni(1)-O(39)	87.1(5)	N(3)-Ni(1)-O1W	167.7(5)
N(2)-Ni(1)-N(2)	95.7(5)	N(3)-Ni(1)-N(1)	100.7 (6)
N(3)-Ni(1)-N(4)	81.8(6)	N(1)-Ni(1)-O(39)	93.5(5)
N(1)-Ni(1)-O1W	87.6(5)	N(1)-Ni(1)-N(2)	80.3(6)
N(1)-Ni(1)-N(4)	177.3(6)	N(5)-Ni(2)-N(6)	81.4(6)
N(5)-Ni(2)-O(8)#1	99.1(5)	N(8)-Ni(2)-O(8)#1	99.1(5)
N(8)-Ni(2)-O(40)	93.5(5)	N(8)-Ni(2)-N(5)	176.7(6)
N(8)-Ni(2)-N(7)	82.5(6)	N(8)-Ni(2)-N(6)	95.5(6)
N(7)-Ni(2)-O(8)#1	85.2(5)	N(7)-Ni(2)-O(40)	174.5(5)
N(7)-Ni(2)-N(5)	98.5(6)	N(7)-Ni(2)-N(6)	87.1(5)
N(6)-Ni(2)-O(8)#1	172.3(5)	O(40)-Ni(2)-N(6)	97.1(5)

Symmetry codes: #1 1-x, 2-y, 1-z

Compound **3**

Co(1)-N(1)	2.148(12)	Co(1)-N(2)	2.193(12)
Co(1)-N(3)	2.127(13)	Co(1)-N(4)	1.916(5)
Co(1)-O(10)#1	2.281(9)	Co(1)-O(19)	2.130(9)
Co(2)-N(5)	2.170(10)	Co(2)-N(6)	2.137(12)

Co(2)-N(7)	2.126(11)	Co(2)-N(8)	2.185(12)
Co(2)-O(25)	2.180(9)	Co(2)-O3W	2.129(10)
C(21)-C(22)	1.35(2)	C(21)-C(20)	1.446(19)
C(7)-C(8)	1.47(2)	C(2)-C(1)	1.49(2)
N(1)-Co(1)-N(2)	79.8(4)	N(4)-Co(1)-N(2)	96.7(4)
N(4)-Co(1)-N(1)	176.5(4)	N(3)-Co(1)-N(1)	99.4(5)
N(3)-Co(1)-N(4)	80.3(5)	N(3)-Co(1)-N(2)	85.8(4)
N(2)-Co(1)-O(10)#1	171.4(4)	N(3)-Co(1)-O(10)#1	86.1(4)
N(4)-Co(1)-O(10)#1	84.4(4)	N(4)-Co(1)-O(19)	95.7(4)
N(3)-Co(1)-O(19)	175.2(4)	N(3)-Co(1)-N(1)	99.4(5)
N(3)-Co(1)-N(4)	80.3(5)	N(3)-Co(1)-N(2)	85.8(4)
N(5)-Co(2)-N(8)	178.2(5)	N(5)-Co(2)-O(25)	93.3(4)
N(6)-Co(2)-N(5)	79.2(4)	N(6)-Co(2)-N(8)	101.4(4)
N(7)-Co(2)-N(5)	102.5(5)	N(7)-Co(2)-N(6)	95.4(5)
N(7)-Co(2)-N(8)	79.1(5)	N(7)-Co(2)-O(25)	86.8(4)

Symmetry codes: #1 1-x, 1-y, 1-z

Compound **4**

Co(1)-N(1)	2.08(3)	Co(1)-N(2)	2.15(3)
Co(1)-N(3)	2.18(3)	Co(1)-N(4)	2.13(3)
Co(2)-N(5)	2.20(3)	Co(2)-N(6)	2.14(3)
Co(2)-N(7)	2.12(3)	Co(2)-N(8)	2.23(3)
Co(2)-O(13)	2.24(2)	Co(2)-O1W	2.09(2)
C(7)-N(2)	1.32(4)	C(7)-C(8)	1.42(5)
C(29)-C(28)	1.46(5)	C(29)-N(8)	1.34(4)
C(2)-C(1)	1.48(5)	C(13)-C(12)	1.41(6)
C(13)-C(14)	1.39(5)	N(2)-C(5)	1.43(5)
N(1)-Co(1)-O(40)	95.1 (10)	N(1)-Co(1)-N(4)	176.8(11)
N(1)-Co(1)-N(3)	99.4(13)	N(1)-Co(1)-N(2)	78.9(11)
N(4)-Co(1)-O(23)#1	100.0(11)	N(4)-Co(1)-N(3)	77.5(13)

N(4)-Co(1)-N(2)	101.9(12)	N(3)-Co(1)-O(23)#1	171.0(9)
N(2)-Co(1)-O(23)#1	83.2(9)	N(2)-Co(1)-N(3)	88.8(11)
N(7)-Co(2)-N(6)	94.6(10)	N(7)-Co(2)-N(8)	77.1(12)
N(7)-Co(2)-N(5)	105.0(12)	N(6)-Co(2)-N(8)	101.8(11)
N(6)-Co(2)-N(5)	79.2(11)	N(5)-Co(2)-N(8)	177.7(12)
N(5)-Co(2)-O(13)	93.8(10)	N(8)-Co(2)-O(13)	85.2(9)

Symmetry codes: #1 1-x 1-y 1-z

Compound **5**

B(1)-O(20)	1.529(5)	B(1)-O(21)	1.534(5)
Cu(1)-N(2)#2	1,999(5)	Cu(1)-N(4)	1.979(4)
Cu(1)-N(5)	1.978(5)	Cu(1)-O(1)	2.275(3)
Cu(1)-O1W	2.035(3)	N(1)-C(4)	1.355(7)
O1W-Cu(1)-O(1)	89.94(14)	N(2)-Cu(1)-O(1)#2	91.07(16)
N(4)-Cu(1)-O(1)	103.96(16)	N(4)-Cu(1)-O1W	166.02(17)
N(4)-Cu(1)-N(2)#2	94.56(19)	N(5)-Cu(1)-O(1)	96.99(19)
N(5)-Cu(1)-O1W	87.01(17)	N(5)-Cu(1)-N(4)	89.79(19)
B(1)-O(21)-W2#1	125.2(2)	B(1)-O(21)-W3#1	126.6(2)

Symmetry codes: #1 1-y,-x,1/2-z; #2 x, +x-y, 1/2-z;

Table S3. Comparison of the electrochemical sensing performance with other electrodes for potassium nitrite.

CPE	Method	Response time	Concentration range	Sensitivity	Correlation	Detection limit	Ref.
1–CPE	Amperometry	1.1s	0.004–0.088 mM	155.5371 μA mM^{-1}	0.99321	1.39×10^{-4} M	This work
2–CPE	Amperometry	1.53s	0.004–0.088 mM	41.20794 μA mM^{-1}	0.99807	1.32×10^{-5} M	This work
3–CPE	Amperometry	1.17s	0.008–0.084 mM	44.35789 μA mM^{-1}	0.99154	3.18×10^{-5} M	This work
4–CPE	Amperometry	1.18s	0.004–0.084 mM	226.2428 μA mM^{-1}	0.99869	4.093×10^{-4} M	This work
5–CPE	Amperometry	1.27s	0.004–0.064 mM	266.6427 μA mM^{-1}	0.99932	3.64×10^{-4} M	This work
CR–GO/GCE	Amperometry	5s	0.0089–0.167 mM	0.0267 μA mM^{-1}	0.09	1.0×10^{-6} M	**11**
6–CPE	Amperometry	2.9s	0.008–0.092 mM	1.074 μA mM^{-1}	0.9986	1.7×10^{-6} M	**12**

Table S4. Comparison of the CO_2RR catalytic performance with other electrodes for CO production.

Catalyst	Potential (V vs. RHE)	Electrolyte	Products	FE (%)	Ref.
1	-1.2	0.5 M $KHCO_3$	CO	47.9	This work
2	-0.9	0.5 M $KHCO_3$	CO	86.3	This work
3	-0.6	0.5 M $KHCO_3$	CO	61.2	This work
4	-0.9	0.5 M $KHCO_3$	CO	38.1	This work
5	-1.1	0.5 M $KHCO_3$	CO	37.6	This work
Cu-ACs/NPC	-0.5	0.5 M $KHCO_3$	CO	93.21	**13**

Cu-N2/GN	-0.5	0.1 M $KHCO_3$	CO	81	**14**
Cu-N4/GN	-0.5	0.1 M $KHCO_3$	CO	62	**14**
Cu-N-C	-0.66	0.5 M $KHCO_3$	CO	21	**15**

Table S5. Comparison of the catalytic performance with other materials for Cr(VI) solution.

Catalyst(mg)	temperature (℃)	time	conversion	Ref.
1 (20mg)	50	60 min	57.3%	This work
2 (20mg)	50	60 min	79.5%	This work
3 (20mg)	50	60 min	76.4%	This work
4 (20mg)	50	60 min	60.5%	This work
5 (20mg)	50	60 min	35%	This work
1 (50mg)	55	120 min	99%	**16**
2 (50mg)	55	180 min	40%	**16**
1 (20mg)	45	70 min	77.6%	**17**
3(20mg)	50	210 min	70%	**18**

References

[1] Yang, H. -B.; Hung, S.-F.; Liu, S.; Yuan, K.; Miao, S.; Zhang, L.; Huang, X.; Wang, H.-Y.; Cai, W.; Chen, R.; Gao, J.; Yang, X.; Chen, W.; Huang, Y.; Chen, H. -M.; Li, C. -M.; Zhang, T.; Liu, B. Atomically dispersed Ni(I) as the active site for electrochemical CO_2 reduction, *Nat. Energy,* **2018**, *3*, 140-147.

[2] Sha, J. -Q.; Peng, J.; Zhang, Y.; Pang, H. -J.; Tian, A. -X.; Zhang, P. -P.; Liu, H. Assembly of Multiply Chain-Modified Polyoxometalates: From One- to Three-Dimensional and from Finite to Infinite Track. *Cryst. Growth & Des.* **2009**, *9*, 1708-1715.

[3] Tian, A. -X.; Liu, J. -N.; Li, T. -T.; Tian, Y.; Liu, G. -Y.; Ying, J. Amperometric sensing and photocatalytic properties under sunlight irradiation of a series Keggin-Ag^I compounds through tuning single and mixed ligands. *CrystEngComm.* **2018**, *20*, 2940-2951.

[4] Dang, D. -B.; Yan, B.; He, C.; Wang, J.; Duan, C. -Y.; Niu, J. -Y. Structure and Catalytic Performance of a Polyoxometalate-Based Metal-Organic Framework Having a Lanthanide Nanocage as a Secondary Building Block. *Inorg. Chem.*

2010, *49*, 1280-1282.

[5] Notash, B.; Safari, N.; Abedi, A.; Amani, V.; Khavasi, H. -R. Cadmium(II) complexes containing 2,2'-dimethyl-4,4'-bithiazole ligand: Synthesis, characterization, and crystal structure. *J. Coord. Chem.* **2009**, *62*, 1638-1649.

[6] Tian, A. -X.; Yang, Y.; Ying, J.; Li, N.; Lin, X. -L.; Zhang, J. -W.; Wang, X. -L. The key role of -CH3 steric hindrance in bis-(pyrazolyl) ligand on polyoxometalate-based compounds. *Dalton Trans.* **2014**, *43*, 8405-8413.

[7] Wang, P.; Wang, X. -P.; Jing, X. -Y.; Zhu, G. -Y. Sol-gel-derived, polishable, 1:12-phosphomolybdic acid-modified ceramic-carbon electrode and its electrocatalytic oxidation od ascorbic acid. *Anal. Chim. Acta.* **2000**, *424*, 51-56.

[8] Zhou, W. -L.; Peng, J.; Zhang, Z. -Y.; Shi, Z. -Y.; Khan, S. -U.; Liu, H. -S. Assembly of hybrids based on polyoxotungstates and Co-tris(imidazolyl) complexes with bifunctional electrocatalytic activities. *RSC Adv.* **2015**, *5*, 35753-35759.

[9] Zhao, J. -W.; Li, Y. -Z.; Ji, F.; Yuan, J.; Chen, L. -J.; Yang, G. -Y. Syntheses, structures and electrochemical properties of a class of 1-D double chain polyoxotungstate hybrids $[H_2bdp][Cu(dap)_2]_{0.5}[Cu(dap)_2(H_2O)][Ln(H_2O)_3(\alpha\text{-}GeW_{11}O_{39})]\cdot 3H_2O$. *Dalton Trans.* **2014**, *43*, 5694-5706.

[10] Xin, X.; Hu, N.; Ma, Y. -Y.; Wang, Y. -L.; Hou, L.; Zhang, H.; Han, Z. -G. Polyoxometalate-based Crystalline Material as Highly Sensitive Electrochemical Sensor for Detecting Trace Cr(VI). *Dalton Trans.* **2020**, *49*, 4570-4577.

[11] Mani, V.; Periasamy, A. -P.; Chen, S. -M.; *Electrochemistry Communications,* 2012, **17**, 75-78.

[12] Tian, A. -X.; Yang, M. -L.; Fu, Y. -B.; Ying, J.; Wang, X. -L.; *Inorg. Chem.,* 2019, **58**, 4190-4200.

[13] Gao, J.; Wang, H.; Feng, K.; Xiang, C. -S.; Wang, H. -B.; Qi, H. -H.; Liu, Y.; Tian, H.; Zhong, J.; Kang, Z. -H.; *Mater. Adv.,* 2020, **1**, 2286-2292.

[14] Zheng, W.; Yang, J.; Chen, H.; Hou, Y.; Wang, Q.; Gu, M.; He, F.; Xia, Y.; Xia, Z.; Li, Z.; Yang, B.; Lei, L.; Yuan, C.; He, Q.; Qiu, M.; Feng, X.; *Adv. Funct. Mater.,* 2020, **30**, 1907658.

[15] Roy, A.; Hursan, D.; Artyushkova, K.; Atanassov, P.; Janaky, C.; Serov, A.; *Appl. Catal. B. Environ.,* 2018, **232**, 512-520.

[16] Xin, X.; Tian. X. -R.; Yu, H. T.; Han, Z. -G. *Inorg. Chem.,* 2018, **18**, 11474-11481.

[17] Tian, X. -R.; Lin, H.; Wang, J. -J.; Xin. X.; Zhang, H.; Ma, Y. -Y.; Wang, Y. -L.; Zhang, L. -N.; Han, Z. -G. *Dalton Trans.,* 2018, **47**, 15121-15130.

[18] Gong, K. -N.; Wang, W. -J.; Yan, J. -S.; Han, Z. -G. *J. Mater. Chem. A.,* 2015, **3**, 6019-6027.